aerospace

MDPI

Article

Analysis of Preliminary Impulsive Trajectory Design for Near-Earth Asteroid Missions under Approaching Phase Constraints

Pureum Kim and Sang-Young Park *

Department of Astronomy, Yonsei University, Seoul 03722, Republic of Korea; prmkim@yonsei.ac.kr
* Correspondence: spark624@yonsei.ac.kr

Abstract: This study investigates the preliminary trajectory design for high-thrust missions to near-Earth asteroids (NEAs), considering distance and phase angle constraints during the approaching phase to enable pre-rendezvous optical navigation and the scientific identification of asteroids. A global optimization algorithm called monotonic basin hopping is used to design Δv-optimal impulsive trajectories both with and without constraints. Comparisons reveal that extending the final leg of the unconstrained reference trajectory and incorporating a few deep-space maneuvers in that final leg can yield a constrained trajectory with a Δv increase of only a few percent. The effects of the phase angle and minimum distance constraint on Δv are also examined. The results indicate that in Δv-optimal constrained trajectories, an additional deep-space maneuver enables the redistribution of maneuvers in the last leg to ideally insert the spacecraft into the constraint cone. However, additional small maneuvers may be necessary at times to ensure that the spacecraft remains within the cone. Based on these findings, we present a two-step approach for the preliminary design of constrained trajectories for NEA missions based on global optimization algorithms. This approach serves as a valuable tool for initial mission design and trade-off analyses involving constraints, fuel usage, and transfer durations.

Keywords: preliminary trajectory design; impulsive trajectory; near-Earth asteroid; close approach to small celestial bodies

check for updates

Citation: Kim, P.; Park, S.-Y. Analysis of Preliminary Impulsive Trajectory Design for Near-Earth Asteroid Missions under Approaching Phase Constraints. *Aerospace* **2023**, *10*, 855. https://doi.org/10.3390/aerospace10100855

Academic Editor: Angelo Cervone

Received: 21 July 2023
Revised: 17 August 2023
Accepted: 26 September 2023
Published: 29 September 2023

1. Introduction

Preliminary trajectory design is a critical step in the planning of interplanetary missions. The selection of an optimal interplanetary transfer trajectory has a direct impact on key mission parameters, such as the Δv requirement, characteristic energy (C_3), and transfer duration, which in turn directly affect the mission's cost and feasibility. Additionally, the interplanetary trajectory is closely linked to other mission aspects, including the spacecraft bus and its subsystems' configuration, as well as the scientific objectives of the mission. In some cases, the trajectory design imposes constraints on these factors, while in others, it is influenced by them. As such, preliminary trajectory design plays a pivotal role in the early stages of mission planning and in the initial assessment of mission feasibility.

Numerous studies have addressed the preliminary trajectory design of interplanetary missions. There are a few major approaches for preliminary trajectory design/optimization, with the propulsion type of the spacecraft engine (low-thrust or high-thrust) mainly determining the applicability of these approaches [1,2]. This study focuses specifically on high-thrust chemical propulsion engines (such as mono- or bi-propellant engines). Due to the very short burn durations (compared to the overall transfer duration) associated with high-thrust trajectories, the impulsive thrust assumption can be utilized during the preliminary trajectory design process for spacecraft equipped with high-thrust engines, with only a minimal loss of fidelity.

A direct method based on the use of global optimization algorithms to solve nonlinear programming problems (NLP) has advantages when designing impulsive interplanetary trajectories involving gravity assists. In this approach, impulsive trajectories are transcribed into finite-dimensional NLPs, and the globally optimal solution (that is, optimal decision variables that minimize or maximize the given cost function) is searched using global optimization algorithms. There are several well-known interplanetary trajectory transcription models, such as the multiple gravity assist (MGA) model [3,4] and the MGA model with one deep-space maneuver per leg (MGA-1DSM) [3–5]. Although global optimization algorithms have several disadvantages, including a low probability of reaching global optimality (often caused by failing to escape from local optima), the heavy multimodality of interplanetary trajectory design problems renders this approach appealing. Furthermore, when compared with indirect methods, it is more straightforward to introduce arbitrary path constraints using methods such as the penalty method [6,7]. Consequently, multiple studies have been conducted to solve impulsive interplanetary trajectory design problems using diverse global optimization algorithms. A few algorithms, such as monotonic basin hopping (MBH), differential evolution (DE), and their derivative algorithms, have been shown to be time-efficient for solving these problems [8–11]. Meanwhile, other algorithms demonstrated advantages in different facets of these trajectory design problems; for instance, the hidden gene genetic algorithm was proven to be capable of solving several subproblems involving a different number of gravity assists and different gravity assist sequences within a single problem [12].

One current trend in interplanetary exploration is the increased interest in missions to near-Earth asteroids (NEAs), as evidenced by several recent and near-future missions, such as Hayabusa (2003, low-thrust) [13], Hayabusa-2 (2014, low-thrust) [14], OSIRIS-REx (2016, high-thrust) [15–17], DART (2021, both high- and low-thrust) [18], Hera (high-thrust) [19], and DESTINY+ (low-thrust) [20]. Other than the scientific value of these asteroids, a reason for their popularity as mission targets lies in the relative ease with which they may be visited. Transfer trajectories to NEAs with low orbital inclinations are often feasible with a single gravity assist from a nearby planet (Earth, Venus, or Mars), or sometimes with only a few deep-space maneuvers (DSMs) without any gravity assist [21].

Most NEAs are much smaller than traditional interplanetary mission targets. For instance, all targets of recent NEA missions, namely Itokawa, Ryugu, Bennu, and Didymos, measure just several hundred meters. Their small sizes make it difficult to acquire precise information (such as size, mass, and shape) from ground-based observations prior to a mission. For this reason, it is effective to introduce the concept of an approaching phase, where the spacecraft approaches the target asteroid slowly, in the final part of the interplanetary transfer. The most basic requirements for this approaching phase trajectory are specified by the spacecraft–asteroid distance and phase angle (an angle between the asteroid–Sun line and asteroid–spacecraft line), so that optical cameras can detect the target asteroid and gather information en route. Such an approaching phase can assist in precise relative orbit determination, trajectory correction, crude asteroid mapping, and the pre-rendezvous identification of significant scientific information (e.g., standard gravitational parameters and the rotational state) [16]. For example, OSIRIS-REx adopted a series of four maneuvers called asteroid approach maneuvers during its Bennu-approaching phase so that the spacecraft could gently approach the asteroid and fully utilize pre-rendezvous optical navigation [17].

Naturally, its significance has spawned several recent studies on the design of approaching phase trajectories toward small celestial bodies. Wang et al. [22] and Qiao et al. [23] presented guidance strategies that can be utilized for low-thrust missions. Wang et al. studied a time-fixed glideslope method for robust rendezvous, while Qiao et al. presented a methodology for designing approaching trajectories that can improve optical navigation performance (observability). Meanwhile, Yuan et al. [24] presented a modified multipulse glideslope method for approaching phase guidance that can improve optical navigation observability, which is suitable for autonomous high-thrust asteroid missions.

However, these studies can only offer partial insights when it comes to estimating the degree to which such an approaching phase trajectory update affects the overall trajectory or propellant use, which may need to be assessed during preliminary mission design and reflected in the design outputs, such as the propellant budget. Therefore, this study focuses on the preliminary design of fuel-optimal high-thrust trajectories from Earth to NEAs, with the basic requirements for optical camera use during the approaching phase being considered as constraints. The basic concept of the problem dealt with in this paper is given in Figure 1. Unconstrained fuel-optimal solutions obtained via frequently used trajectory models such as MGA and MGA-1DSM (red trajectories in Figure 1) are likely to approach the target asteroid from an arbitrary phase angle at a high relative speed, both of which can make pre-rendezvous optical camera use challenging or even impossible. The reference unconstrained trajectory can be updated to accommodate the approaching phase without further optimization, i.e., by adding a deep space maneuver whose timing and location are fixed to desired values (orange trajectories in Figure 1). However, such an approaching trajectory guarantees neither fuel-optimality nor the satisfaction of the approaching phase constraints, especially if the desired distance at which the spacecraft begins optical camera use is far from the asteroid. For this reason, further optimization may be necessary so as to find a fuel-optimal trajectory that also satisfies the approaching phase constraints (blue trajectories in Figure 1).

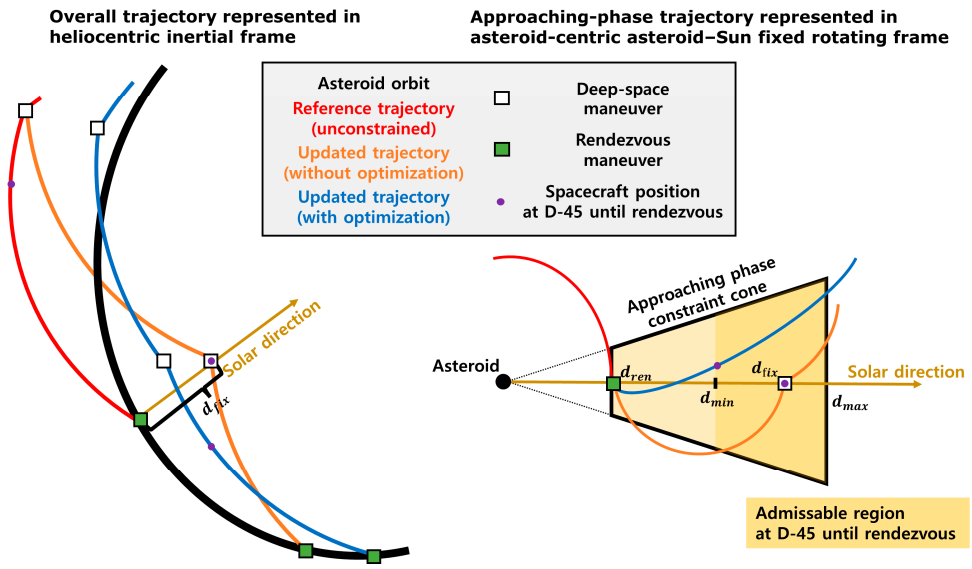

Figure 1. The problem description of the current study.

Accordingly, the main aims of this study are (a) to determine the characteristics of Δv-optimal constrained trajectories, (b) to quantify the effects of these constraints on Δv and the transfer duration, and (c) to present an efficient method of designing a constrained trajectory from a baseline reference trajectory, based on the results obtained. In order to mitigate the possibility of missing a feasible optimal constrained solution, the current study is structured in a way that begins with searching for solutions with more freedom in design (in terms of decision variable bounds and the number of impulses), but incrementally diminishes the size of the search space by identifying critical parameters that bring about differences between unconstrained and constrained solutions. Also, in order to accommodate the infinite possibilities of geometry, the trajectory optimization procedure is performed for 20 selected NEAs. As for the method of optimization, a modified version of the MBH algorithm is used. The analyses presented here may suffer from numerical limitations (such as the solutions being suboptimal) due to the stochastic nature of the methodology, and cannot be fully comprehensive because the number of possible geometries of the planetary bodies and the spacecraft trajectory are infinite. Still, these analyses can provide trajectory designers with a general idea of the effects of the approaching phase constraints on the

fuel-optimal trajectory and allow insights regarding the design or update of trajectories under such restrictions.

The remainder of this paper is organized as follows. In Section 2, several impulsive trajectory models are introduced, and Section 3 presents the modified version of the MBH algorithm used in this study. The list of 20 target NEAs used for the trajectory design analysis, along with the selection criteria, is presented in Section 4. Then, the results and analyses are presented in Sections 5–7, respectively. In Section 5, the minimum number of additional maneuvers required and the critical trajectory parameters for designing constrained trajectories are identified. In Section 6, the effects of changing the last leg duration, which is revealed to be a crucial parameter affecting Δv and the transfer duration, are discussed. In Section 7, the intertwined effects of the minimum distance and the maximum phase angle constraints are discussed. Based on these findings, a two-step preliminary constrained trajectory design approach is proposed in Section 8, and conclusions are presented in Section 9.

2. Impulsive Trajectory Transcription Models

The general form of the optimal control problem is extremely difficult to handle in its original form; thus, several assumptions and approximations are often introduced to simplify the problem into a solvable one. In the field of impulsive interplanetary trajectory design, there are already a few well-known transcription models that convert the optimal control problem into nonlinear programming problems (NLP), such as the n-impulse model [21,25], the multiple gravity assist (MGA) model [3,4], and the MGA model with one deep-space maneuver per leg (MGA-1DSM) [3–5]. In this study, since only a single gravity assist (swing-by) was assumed, the MGA model was excluded from the analysis. The MGA model is more suitable for trajectories involving several gravity assists.

In the following subsections, we formally introduce the n-impulse model and 1GA-1DSM (that is, an MGA-1DSM model with only a single gravity assist), along with its derivative model named 1GA-nDSMt. We also discuss the cost function definitions used in this study and how the approaching phase constraints are reflected in the optimization process in the form of penalty functions. In the last subsection, we introduce the categorization of the trajectory models used throughout this study to avoid confusion in the following sections.

2.1. Dynamic Model

All trajectory transcription models used in this study assumes the use of the zero-sphere-of-influence patched conic method. That is, each planetary body's sphere of influence is reduced to a point located at the center of the planetary body. With this approximation, impulsive trajectory models can be designed by simply connecting heliocentric Keplerian arcs (one of whose foci are at the Sun) with impulses (either by maneuvers or gravity assists) occurring at the ends of the arcs. This approximation is very effective in simplifying the interplanetary trajectory design problem without a significant loss of fidelity, and has been frequently used in preliminary trajectory design stages [3–12,21].

The Keplerian arcs that compose the trajectory can be computed either by solving Lambert's problem or using two-body propagators, depending on the known boundary values for that arc. Hereafter, in this study, we refer to each part of a trajectory that connects two planetary bodies as a leg, and each Keplerian arc as an arc. Naturally, a leg comprises one or more arcs. A deep-space maneuver (DSM) is applied to the spacecraft at a point connecting two arcs of the same leg. On the other hand, a gravity assist occurs at a point connecting two legs.

One small exception to the forementioned assumption is the definition of an asteroid rendezvous. In this study, the asteroid rendezvous is defined as reaching the 10 km distance from the center of the target asteroid in the direction of the Sun (that is, $d_{ren} = 10$ km in Figure 1) and possessing the same heliocentric velocity as that of the asteroid. Another point of mention is the perturbing forces acting on the spacecraft during the approaching

phase. Even at the 10 km distance, the acceleration acting on the spacecraft is dominated by solar gravity for most near-Earth asteroids (NEA); for example, the spacecraft located 10 km away from Ryugu (the most massive among the four NEAs visited) should experience accelerations owing to Ryugu's point-mass gravity and solar radiation pressure (two major perturbation sources), which are smaller than the solar gravitational acceleration by more than four orders of magnitude. Based upon this, the approaching phase trajectory still assumes the effect of the solar gravitational force only in this study.

2.2. *n*-Impulse Model

n-impulse models are impulsive trajectory models that rely on impulsive maneuvers without assistance from gravity assists, where n denotes the total number of impulses along the trajectory. For rendezvous problems, the minimum number of impulses required is two, which corresponds to the solution obtained by solving Lambert's problem. For models with $n \geq 3$, the model involves $n - 2$ DSMs. The resultant trajectory consists of a single leg composed of $n - 1$ arcs. In this study, the two-impulse model (solution to Lambert's problem) is disregarded, and the focus is put on cases where $3 \leq n \leq 5$.

The three-impulse model is illustrated in Figure 2a. In all the trajectory model illustrations in Figure 2, the thick green arrows refer to arcs computed via two-body propagation, with arrows pointing towards the direction of propagation, while the thick blue lines refer to arcs computed via solving Lambert's problem. When solving Lambert's problem, we used only a counterclockwise solution with zero full revolutions. The definition of each leg is represented by gray dotted lines.

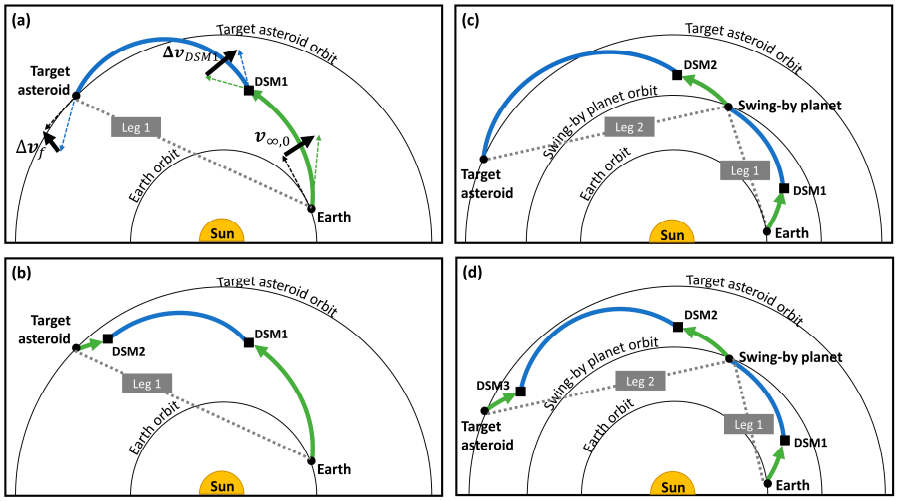

Figure 2. Simplified illustration for the (**a**) 3-impulse model, (**b**) 4-impulse model, (**c**) 1GA-2DSMt model, and (**d**) 1GA-3DSMt model.

The three-impulse model is defined by six decision variables, and in the form of the corresponding decision vector, $\boldsymbol{D}_3$, it is represented as follows:

$$\boldsymbol{D}_3 = \begin{bmatrix} t_0 & T_1 & \eta_{1,a} & v_{\infty,0} & l_{\infty,0} & b_{\infty,0} \end{bmatrix}. \tag{1}$$

The initial time of leaving Earth is denoted by t_0, and the transfer duration of the first (and only) leg is denoted by T_1. To express the time of flight (TOF) for each of the two arcs in the first leg, a proportion variable, $\eta_{1,a} \in [0,\ 1]$, is introduced. The TOF of the first and second arcs, which are respectively denoted by $T_{1,1}$ and $T_{1,2}$, can be computed as follows:

$$T_{1,1} = \eta_{1,a} T_1,\ T_{1,2} = (1 - \eta_{1,a}) T_1, \tag{2}$$

where the first number in the subscript refers to the leg number and the second number refers to the arc number within that leg.

Finally, the remaining three variables are used to express the hyperbolic excess velocity vector of the spacecraft leaving Earth. $v_{\infty,\,0} = \sqrt{C_{3,0}}$ is the magnitude of the vector, whereas $l_{\infty,\,0}$ and $b_{\infty,\,0}$ represent the ecliptic longitude and latitude of the vector direction, respectively. The post-impulse velocity vector of the spacecraft in the heliocentric ecliptic inertial (HCI) frame can be computed as follows:

$$\boldsymbol{v}_0^+ = \boldsymbol{v}_0^- + \boldsymbol{v}_{\infty,0} = \boldsymbol{v}_0^- + v_{\infty,0} \begin{bmatrix} \cos(b_{\infty,0})\cos(l_{\infty,0}) \\ \cos(b_{\infty,0})\sin(l_{\infty,0}) \\ \sin(b_{\infty,0}) \end{bmatrix}, \tag{3}$$

where $\boldsymbol{v}_0^-$ is the Earth's velocity vector in the HCI frame at t_0. In addition, $\boldsymbol{r}_0$ (the initial position vector of the spacecraft in the HCI frame) equals Earth's position vector in the HCI frame at the initial time, t_0, according to the zero-sphere-of-influence approximation. Therefore, the initial post-impulse state is as follows:

$$\boldsymbol{X}_0^+ = \begin{bmatrix} \boldsymbol{r}_0 \\ \boldsymbol{v}_0^+ \end{bmatrix}. \tag{4}$$

Similarly, the pre- and post-impulse state vectors at the final time $t_f = t_0 + T_1$ are represented by the following:

$$\boldsymbol{X}_f^- = \begin{bmatrix} \boldsymbol{r}_f \\ \boldsymbol{v}_f^- \end{bmatrix}, \boldsymbol{X}_f^+ = \begin{bmatrix} \boldsymbol{r}_f \\ \boldsymbol{v}_f^+ \end{bmatrix}, \tag{5}$$

where the post-impulse subvectors, $\boldsymbol{r}_f$ and $\boldsymbol{v}_f^+$, should be equal to the target asteroid position and velocity in the HCI frame at the final time under the same principle. However, as stated in Section 2.1, we assumed that the final spacecraft position, $\boldsymbol{r}_f$, is located 10 km away from the center of the asteroid in the direction of the Sun.

Now that all the boundary values are defined, we connect the boundary states with two arcs. As shown in Figure 2a, the first arc is computed by propagating the orbital state vectors, $\boldsymbol{X}_0^+$, for the duration of $T_{1,1}$, which results in the propagated state vector, $\boldsymbol{X}_{1,1}^-$. Because the initial and final positions for the second arc ($\boldsymbol{r}_{1,1}$ and $\boldsymbol{r}_f$) and the TOF of that leg ($T_{1,2}$) are now known, the second arc can be obtained from a Lambert solver, which yields $\boldsymbol{v}_{1,1}^+$ and $\boldsymbol{v}_f^-$. With both arcs fully defined, the impulsive thrust vectors for the DSM, $\Delta\boldsymbol{v}_{DSM1}$, and the final rendezvous maneuver, $\Delta\boldsymbol{v}_f$, can be easily obtained as follows:

$$\Delta\boldsymbol{v}_{DSM1} = \boldsymbol{v}_{1,1}^+ - \boldsymbol{v}_{1,1}^- \tag{6a}$$

$$\Delta\boldsymbol{v}_f = \boldsymbol{v}_f^+ - \boldsymbol{v}_f^-. \tag{6b}$$

In fact, for missions to planets and massive asteroids, the orbital insertion burn magnitude should be computed considering the insertion orbit; however, for small asteroids, we can simply assume that Equation (6b) holds, at least during the preliminary design phase. Figure 2a shows the graphical definitions of $\boldsymbol{v}_{\infty,0}$, $\Delta\boldsymbol{v}_{DSM1}$, and $\Delta\boldsymbol{v}_f$ with thick black arrows, which are the vector differences between the thin dotted arrows representing the pre- and post-impulse velocity vectors. For simplicity, these velocity and impulse vectors are omitted from the other trajectory model illustrations.

The four- and five-impulse models can be constructed in a similar manner. The four-impulse model is shown in Figure 2b. For the four-impulse model, the last arc is obtained by back-propagating the pre-impulse orbital state vector at the final time. For the five-impulse model, the last two arcs are obtained via sequential backpropagation. The reason for such backpropagation is to allow the magnitude of the final rendezvous maneuver to be encoded in the decision vectors, which should be small for trajectories with approaching phase constraints; thus, it is more straightforward for trajectory designers to set tight bounds on this variable after some test runs. The two models require 10 and

14 variables to define a trajectory solution. The decision vectors, denoted as $\boldsymbol{D}_4$ and $\boldsymbol{D}_5$, respectively, are given below:

$$\boldsymbol{D}_4 = \begin{bmatrix} t_0 & T_1 & \eta_{1,a} & \eta_{1,b} & v_{\infty,0} & l_{\infty,0} & b_{\infty,0} & \Delta v_f & l_f & b_f \end{bmatrix} \tag{7a}$$

$$\boldsymbol{D}_5 = \begin{bmatrix} t_0 & T_1 & \eta_{1,a} & \eta_{1,b} & \eta_{1,c} & v_{\infty,0} & l_{\infty,0} & b_{\infty,0} & \Delta v_f & l_f & b_f & \Delta v_{DSM3} & l_{DSM3} & b_{DSM3} \end{bmatrix} \tag{7b}$$

The computation of $\Delta \boldsymbol{v}$ vectors (for $\Delta \boldsymbol{v}_f$ and $\Delta \boldsymbol{v}_{DSM3}$) can be performed in the same manner as that in Equation (3), simply by replacing $v_{\infty,0}$ with Δv_f or Δv_{DSM3} along with their corresponding ecliptic longitude and latitude values. The TOF of each arc can be computed from Equation (8a) for the four-impulse model, and from (8b) for the five-impulse model:

$$T_{1,1} = T_1\eta_{1,a}, T_{1,2} = T_1(1-\eta_{1,a})\eta_{1,b}, T_{1,3} = T_1(1-\eta_{1,a})(1-\eta_{1,b}) \tag{8a}$$

$$\begin{gathered} T_{1,1} = T_1\eta_{1,a}\eta_{1,b}, T_{1,2} = T_1\eta_{1,a}(1-\eta_{1,b}) \\ T_{1,3} = T_1(1-\eta_{1,a})\eta_{1,c}, T_{1,4} = T_1(1-\eta_{1,a})(1-\eta_{1,c}). \end{gathered} \tag{8b}$$

2.3. 1GA-1DSM and 1GA-nDSMt Model

The MGA-1DSM model can include multiple gravity assists, but only single swing-by trajectories were investigated in this study; therefore, we simply refer to this model as 1GA-1DSM. The 1GA-1DSM model consists of two legs, each of which contains a single DSM, resulting in two DSMs in total. Figure 2c illustrates the 1GA-1DSM model. The decision vector for this model consists of 10 decision variables as follows:

$$\boldsymbol{D}_{1GA-1DSM} = \begin{bmatrix} t_0 & T_1 & T_2 & \eta_{1,a} & \eta_{2,a} & v_{\infty,0} & l_{\infty,0} & b_{\infty,0} & R_1 & \theta_1 \end{bmatrix}. \tag{9}$$

The initial time, t_0, and three hyperbolic excess velocity vector variables ($v_{\infty,0}$, $l_{\infty,0}$, and $b_{\infty,0}$) have the same physical meaning as they do in the n-impulse models. The four decision variables related to the time duration (T_1, T_2, $\eta_{1,a}$, and $\eta_{2,a}$) can be used to compute the time duration for each arc in the same manner as in Equation (2). The last two decision variables, R_1 and θ_1, are required to define the first (and only) swing-by. Here, R_1 denotes the minimum distance between the spacecraft and planet during the swing-by, and θ_1 is the incoming B-plane angle. There are a few different ways to compute the post-swing-by heliocentric velocity of the spacecraft from the pre-swing-by velocity and these two decision variables; the method used here is based on Kawakatsu's approach [26]. Note that although the gravity-assist planet is not encoded in the decision vector as a variable, it should be selected for the trajectory to be defined. The remainder of the process, which is basically linking the boundary conditions with Keplerian arcs, can be performed in the same manner as with the n-impulse models.

The derivative model, 1GA-nDSMt, where n refers to the *total* number of DSMs along the entire transfer, differs from the original 1GA-1DSM model in that more than one DSM may be allowed in the *last* leg of the trajectory, whereas the first leg still allows only one DSM. We only consider cases in which the number of DSMs in the last leg ranges from one to three (or equivalently, $2 \leq n \leq 4$); when it equals one, it is simply the original 1GA-1DSM model. For example, the 1GA-3DSMt model is illustrated in Figure 2d. For the sake of unity, we refer to the 1GA-1DSM model as 1GA-2DSMt, which has the decision vector of Equation (9). The decision vectors of 1GA-3DSMt and 1GA-4DSMt, whose problem dimensions are 14 and 18, respectively, are given by

$$\boldsymbol{D}_{1GA-3DSMt} = \begin{bmatrix} t_0 & T_1 & T_2 & \eta_{1,a} & \eta_{2,a} & \eta_{2,b} & v_{\infty,0} & l_{\infty,0} & b_{\infty,0} & \Delta v_f & l_f & b_f & R_1 & \theta_1 \end{bmatrix} \tag{10a}$$

$$\boldsymbol{D}_{1GA-4DSMt} = \begin{bmatrix} t_0 & T_1 & T_2 & \eta_{1,a} & \eta_{2,a} & \eta_{2,b} & \eta_{2,c} & v_{\infty,0} & l_{\infty,0} & b_{\infty,0} & \Delta v_f & l_f & b_f & \Delta v_{DSM4} & l_{DSM4} & b_{DSM4} & R_1 & \theta_1 \end{bmatrix} \tag{10b}$$

In this study, after preliminary tests on three nearby planets (Venus, Earth, and Mars) as potential swing-by planets, we limited the swing-by planets to Venus and Earth. To denote the name of the swing-by planet in the trajectory model, we substituted the number of swing-bys ("1") with the initial letter of the swing-by planet ("E" or "V"). For instance, EGA-3DSMt refers to the 1GA-3DSMt model that uses an Earth swing-by, while VGA-3DSMt refers to the same model that uses a Venus swing-by.

2.4. Cost Function and Penalty Function Definition

In this study, the cost function for the unconstrained optimization was defined as the total Δv magnitude from leaving Earth to the rendezvous with the target asteroid, which must be minimized for fuel optimality. In most interplanetary missions, spacecrafts are placed on an interplanetary trajectory via an injection maneuver performed using a launch vehicle; this burn magnitude is included in the total Δv. The spacecraft was assumed to be injected into the transfer trajectory from a circular Earth parking orbit at an altitude of 500 km. The injection burn magnitude was computed as follows:

$$\Delta v_0 = \sqrt{v_{\infty,0}^2 + \frac{2\mu_E}{(r_E + a_p)}} - \sqrt{\frac{\mu_E}{(r_E + a_p)}}, \tag{11}$$

where μ_E and r_E refer to the standard gravitational parameter and Earth radius, respectively, and a_p is the parking orbit altitude. The total Δv magnitude is the summation of Δv_0, Δv_f, and all DSM magnitudes as follows:

$$J = \Delta v_0 + \Delta v_f + \sum \Delta v_{DSM}. \tag{12}$$

To consider approaching trajectory constraints, we used the penalty function method, which is a commonly used method for constrained global optimization [6,7]. Penalty functions are defined as zero when constraints are satisfied, but possess positive values when violated. These penalty functions were added to the original cost function to form a modified cost function, and the global optimization algorithm sought a solution that minimized the modified cost function.

With respect to the spacecraft–asteroid distance, d, if the constraints on the minimum and maximum distance at some specified time before rendezvous are given by d_{min} and d_{max}, the corresponding penalty function is defined in quadratic form as follows:

$$p_d = \begin{cases} \left(\frac{d-d_{max}}{d_{max}}\right)^2 & d > d_{max} \\ 0 & d_{min} \le d \le d_{max} \\ \left(\frac{d-d_{min}}{d_{min}}\right)^2 & d < d_{min} \end{cases}. \tag{13}$$

The reason for placing the minimum distance limit is to prevent trivial solutions, where the spacecraft rendezvous with the asteroid using the last DSM and follows the asteroid thereafter, with the actual rendezvous maneuver having near-zero magnitude. This phenomenon is discussed in more detail in Section 7.

Similarly, for the phase angle, ϕ, (a non-negative angle between the asteroid–Sun line and asteroid–spacecraft line), if the maximum phase angle constraint at some specified time before rendezvous is given by ϕ_{max}, the corresponding penalty function is defined as

$$p_\phi = \begin{cases} \left(\frac{\phi-\phi_{max}}{\phi_{max}}\right)^2 & \phi > \phi_{max} \\ 0 & \phi \leq \phi_{max} \end{cases}. \tag{14}$$

For the case in which both distance and phase angle constraints are considered, the cost function for constrained optimization is defined as

$$J_p = J + 10000 p_d + 10000 \sum p_\phi, \tag{15}$$

where J is in km/s, while p_d and p_ϕ are unitless quantities. The static penalty coefficients, which are set to 10,000 for both types of penalties, were chosen such that a 1% constraint error corresponds to a 1 km/s penalty, whereas a 2% constraint error corresponds to a 4 km/s penalty. Here, they were set at a high level because one primary objective of this study is to understand the difference between unconstrained and constrained solutions; thus, it was desirable for constrained solutions to satisfy constraints to a great degree. If they had been set at a low level, the optimal solutions found would be ones that are balanced between fuel consumption and constraint violation, which might be acceptable in practical design, but may hamper the objective of this study.

These distance and phase angle constraints are generally required within a few weeks or months before the final rendezvous (defined herein as arriving at 10 km distance from the center of the asteroid with a zero-degree phase angle, as stated in Section 2.1) maneuver. We assumed a situation where the approaching phase constraints should be in effect from D-45 to D-day (the eventual rendezvous date). As for the distance constraint, the asteroid–spacecraft distance monotonically decreases during the last few weeks of interplanetary transfer in general; therefore, we assumed that a single distance check at D-45 would be sufficient. However, the phase angle values may vary significantly as it approaches the rendezvous. Therefore, they should ideally be reflected as path constraints. However, to reduce the computation time for the objective function evaluation, they were checked three times: at D-45, D-30, and D-15. This is reflected in Equation (15) using the sigma notation for p_ϕ.

2.5. Categorization of Trajectory Models

In this subsection, the trajectory models introduced in Sections 2.2 and 2.3 are specified individually, and their two-fold categorization is introduced, the notation of which will be useful in understanding the analyses of the study.

In this study, we considered a total of nine trajectory models, counting different swing-by sequences as constituting different trajectory models. The three come from n-impulse models ($3 \leq n \leq 5$). The remaining six are VGA-nDSMt and EGA-nDSMt models ($2 \leq n \leq 4$). The nine trajectory models were first categorized according to the swing-by planet as no-GA-, VGA-, and EGA-types. This categorization was introduced because when optimized, the three models inside each category should result in similar trajectories with which a fair comparison can be made.

The nine trajectory models were also categorized according to the number of DSMs in the last leg. For instance, three models that have only one DSM in their last legs, namely three-impulse, EGA-2DSMt, and VGA-2DSMt, constitute the 1DSMLL (one deep-space maneuver in the last leg) category, whereas the other six models that have two or three DSMs in their last legs constitute the 2DSMLL and 3DSMLL categories, respectively. It is known that when there are no trajectory constraints, having more than one DSM per leg often does not contribute to a meaningful improvement in fuel usage [10,21,27], indicating that 1DSMLL trajectories are often sufficient for general trajectory design. This is likely the result of the optimal number of impulses being dependent on the number of

revolutions [28], and in high-thrust interplanetary trajectory design, it is uncommon to have a many-revolution trajectory owing to practical limitations in the transfer duration. Therefore, it is natural to use 1DSMLL trajectory models to design reference unconstrained trajectories. However, when we consider approaching phase constraints, having more than one DSM in the last leg may allow for a decrease in fuel usage, and thus 2DSMLL and 3DMSLL trajectories are likely to be more fuel-optimal than 1DSMLL trajectories are. For these reasons, in the following sections, 1DSMLL models are often referred to as reference models, and the unconstrained solutions of these 1DSMLL models are referred to as reference trajectories in the sense that they constitute the baseline to which the other models/trajectories can be compared. Table 1 lists the nine trajectory models according to their two-fold categorization.

Table 1. The nine trajectory models used in this study, categorized by the swing-by sequence and the number of DSMs in the last leg.

	No-GA-Type	**VGA-Type**	**EGA-Type**
1DSMLL-type (Reference models)	3-impulse	VGA-2DSMt	EGA-2DSMt
2DSMLL-type	4-impulse	VGA-3DSMt	EGA-3DSMt
3DSMLL-type	5-impulse	VGA-4DSMt	EGA-4DSMt

3. Modified Monotonic Basin Hopping Algorithm

In this section, we introduce the stochastic optimization algorithm used in this study. Because the algorithm itself is not the focus of the current research, we discuss it only briefly. More detailed information on the algorithm used in this study can be found in Ref. [10].

The MBH algorithm is a stochastic global optimization algorithm that was first proposed in the field of physical chemistry to determine the lowest-energy structure of a molecular system [29]. This algorithm has been found to be efficient in space trajectory design problems [8–10], possibly because of their funnel-structured landscapes [30]. The MBH algorithm aims to locate the global optimum by repeatedly hopping to a better local optimum, where it relies on local optimization algorithms to locate the local optima.

In the modified version of MBH [10] used in this study, there are three major differences when compared with the original algorithm. First, during the initial stage of MBH, we used the multi-start algorithm [31] to locate a good local optimum and set it as the initial starting point for the MBH algorithm. Second, the algorithm was parallelized in the same manner as in [32] because the original MBH algorithm cannot fully utilize current multicore CPUs. Finally, a subroutine for estimating an adequate perturbation size was introduced in the algorithm [10]. Perturbation size is one of the factors that critically affects the MBH algorithm's performance, and this subroutine allows it to be automatically determined to an adequate value without user intervention.

Figure 3 illustrates the simplified procedure of the modified MBH algorithm, which seeks the global minimum of a 1D optimization problem. An initial starting point, represented by the ball with a "0" sign in Figure 3, is chosen by the multi-start algorithm. Randomly generated perturbations are added to this local minimum solution, and the local search algorithm is run in parallel from these perturbed states to locate other local minima. If none of the newly found local minima are better than the currently known best local minimum, this search is ignored (e.g., balls with a "1" sign in Figure 3) and the perturbation size is increased to enable a wider search. However, if a search succeeds in locating a local minimum better than the currently known best one does, an update is made to the best local minimum (e.g., balls with a "2" sign in Figure 3), and an adequate perturbation size is re-calculated to reflect the landscape of the new neighborhood. This search-and-update process continues until a user-defined stopping condition, such as the number of successive search failures or the computation time, is met.

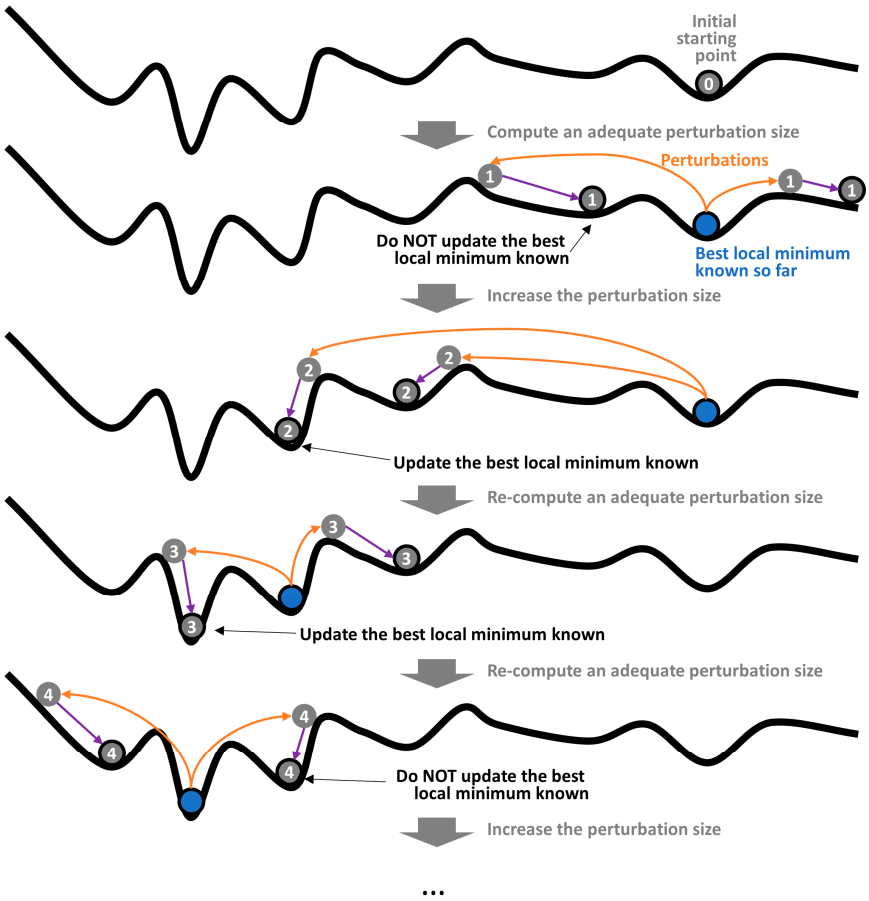

Figure 3. Simplified graphical illustration of the modified monotonic basin hopping algorithm approaching the global optimum for a 1D optimization problem. The numbers written inside the balls refer to the current number of the parallel local search runs.

As the current study relies on a global optimization algorithm to find globally optimal solutions, which are then used to analyze the optimal solutions' characteristics, it is also important to assure that the algorithm used is effective in solving the problems discussed in this study. For this reason, a performance comparison between different global optimization algorithms is briefly discussed below. Four different algorithms, namely the genetic algorithm (GA), particle swarm optimization (PSO), multi-start (MS), and the algorithm used in this study (MBH), were used to solve two different trajectory design problems that will be discussed in Sections 5 and 6. For each problem, each algorithm was run 200 times until the pre-defined computation time was met. The GA and PSO algorithms used are MATLAB built-in functions, while the MS and MBH algorithms are in-house codes. All algorithms were configured to utilize CPU parallelization.

Figure 4a shows the boxplot for the problem of constrained EGA-2DSMt trajectory design for asteroid 2004 XZ130 (one of the 20 target asteroids; refer to Section 4) for a broad search (refer to Section 5.2), while Figure 4b shows that for the problem of constrained EGA-3DSMt trajectory design for the same asteroid with a fixed last leg duration extension (refer to Section 6). Boxplots were drawn such that outliers are not explicitly shown but covered by whiskers. The former problem features a lower dimensionality but wider search space, while the latter problem has a higher dimensionality but narrower search space. As can be seen from both panels, local-optimization-based algorithms (MS and MBH) outperform GA and PSO, and MBH slightly outperforms MS. More comparisons between optimization algorithms for impulsive interplanetary trajectory design can be found in Refs. [8–10].

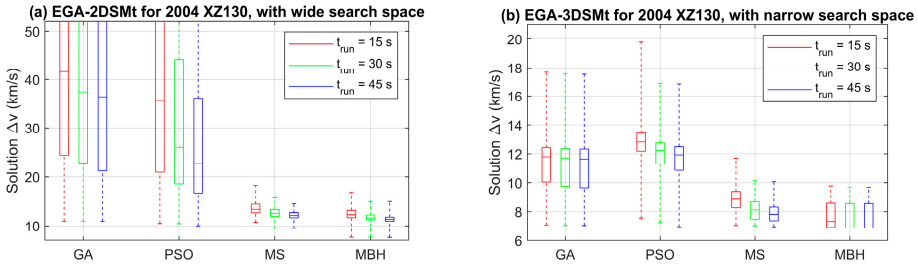

Figure 4. Performance comparison between different global optimization algorithms for two different trajectory design problems covered in this study.

4. Target Asteroid Selection

NEAs are defined as asteroids with a perihelion distance of 1.3 astronomical units (au) or less. NEAs can be categorized into four groups based on their orbital elements: Atiras, Atens, Apollos, and Amors. Atiras are NEAs whose heliocentric orbits are strictly inside Earth's orbit, whereas Amors have orbits strictly outside Earth's orbit. Both Atens and Apollos cross Earth's heliocentric orbit; those with a semi-major axis of less than 1 au are classified as Atens, whereas those with more than 1 au are categorized as Apollos.

We selected 20 NEAs for this study, with five from each orbital group. When choosing the target asteroids from each group, two criteria were applied, so that the analysis performed in this study could be more easily generalized for realistically feasible missions; the orbital inclination should be lower than 15°, and the eccentricity should be lower than 0.5. These two orbital elements, especially the inclination, affect the ease of visiting the asteroid. Because more than five asteroids could satisfy the criteria, we sorted the candidate list by absolute magnitude and selected the five most luminous ones. The luminosity criterion was adopted to prevent selection bias, which may arise from handpicked selection.

The selected NEAs are listed in Table 2 along with their nominal orbital elements obtained from NASA JPL Horizons System [33]. However, when computing their positions and velocities for the simulation, we did not use these nominal elements; instead, high-fidelity ephemerides generated by the same Horizons System was used [34].

Table 2. List of the 20 NEAs selected for trajectory design analysis.

Group	#	Name	Other Name	SPK ID	a (au)	e	i (deg)	Ω (deg)	ω (deg)
Atiras	1	2004 XZ130		2164294	0.6175	0.4546	2.95	211.17	5.4
	2	1998 DK36		3184472	0.6923	0.416	2.02	151.46	180.04
	3	2012 VE46		3617387	0.7131	0.3613	6.67	8.76	190.49
	4	2015 DR215		3712675	0.6666	0.4716	4.06	314.66	42.61
	5	2021 LJ4		54158076	0.6748	0.3834	9.83	277.61	56.89
Atens	6	1998 XB		2096590	0.9078	0.3511	13.6	75.7	202.72
	7	1992 FE		2005604	0.9286	0.4061	4.72	311.9	82.65
	8	2003 SD220		2163899	0.8276	0.2099	8.54	273.74	326.94
	9	1998 WT24		2033342	0.7188	0.4176	7.37	81.67	167.53
	10	2003 UC20		2363505	0.7811	0.3369	3.81	188.3	59.79
Apollos	11	1948 OA	Toro	2001685	1.368	0.436	9.38	274.23	127.21
	12	1951 RA	Geographos	2001620	1.246	0.3354	13.34	337.18	276.97
	13	1999 KV4		2025330	1.54	0.371	14.33	50.54	86.1
	14	1994 CN2		2136618	1.573	0.395	1.44	99.34	248.28
	15	1991 VH		2035107	1.137	0.1442	13.91	139.35	206.95
Amors	16	A898 PA	Eros	2000433	1.458	0.2227	10.83	304.29	178.93
	17	1929 SH	Ivar	2001627	1.863	0.3966	8.45	133.12	167.81
	18	1953 RA	Boreas	2001916	2.272	0.4499	12.88	340.6	335.9
	19	1992 AE	Miwablock	2006050	2.203	0.4371	6.4	88.18	284.98
	20	1977 RA	Beltrovata	2002368	2.105	0.4133	5.22	287.32	43.09

5. General Analysis of Effect of the Constraints

This section presents a general analysis of the effects of introducing approaching phase constraints. Solving both unconstrained and constrained problems separately in the same vast search space and comparing their solutions can reveal the number of additional impulses required and provide insights into how unconstrained fuel-optimal solutions can be efficiently modified into constrained fuel-optimal solutions.

5.1. Broad and Narrow Search Settings

For each asteroid listed in Table 2, unconstrained and constrained optimizations were performed for all nine trajectory models listed in Table 1. Table 3 lists the bounds of the baseline decision variable. During the local search stage of the MBH algorithm, the angular variable bounds are extended by three times the baseline bounds listed in the table, as stated in the table footer. As the optimization problem landscape is infinitely repeated over the angular variables, such bound extensions can prevent the occurrence of unintended premature convergence at the bounds [10]. In terms of constraints, three cases were explored separately:

Table 3. Baseline decision variable bounds.

Applicable Trajectory Models	Decision Variable	Lower Bound	Upper Bound
All	t_0	1 January 2032 00:00:00 UTC	31 December 2034 24:00:00 UTC
	T	150 days	700 days
	η	0.01	0.99
	$v_{\infty,0}$	2 km/s	7 km/s
	$l_{\infty,0}$	–180 degrees [1]	180 degrees [1]
	$b_{\infty,0}$	–90 degrees [2]	90 degrees [2]
2DSMLL-type 3DSMLL-type	Δv_f	0 km/s	0.25 km/s
	l_f	–180 degrees [1]	180 degrees [1]
	b_f	–90 degrees [2]	90 degrees [2]
3DSMLL-type	Δv_{DSM}	0 km/s	1 km/s
	l_{DSM}	–180 degrees [1]	180 degrees [1]
	b_{DSM}	–90 degrees [2]	90 degrees [2]
EGA-type VGA-type	R	1.2 planet radii swing-by	10 planet radii swing-by
	θ	–180 degrees [1]	180 degrees [1]

[1] These angular variable bounds are extended to [–540, 540] degrees during the local search stage of the MBH algorithm. [2] These angular variable bounds are extended to [–270, 270] degrees during the local search stage of the MBH algorithm.

1. No constraints. The corresponding cost function is simply Equation (12).
2. Only distance constraint. The asteroid–spacecraft distance is checked 45 days before the rendezvous, and should lie between 300,000 km (d_{min}, approximately 0.002 au) and 3,000,000 km (d_{max}, approximately 0.02 au). The cost function is given by Equation (15) without the p_ϕ term.
3. Both distance and phase angle constraints. The distance constraint is the same as above, and the additional maximum phase angle constraint is set at 60° (ϕ_{max}) and checked three times at 15, 30, and 45 days before the rendezvous. The cost function is given by Equation (15). For reference, a phase angle of 60° corresponds to an illuminated fraction of 75% under the assumption of spherical asteroids [35].

This section focuses on two different search results; the broad search refers to the broad baseline bound length of the initial time, t_0, to distinguish it from the narrow search, in which the bound length for that variable is shortened to ±15 days of that of the optimal reference solution obtained from the broad search. The two main objectives of the broad search are to identify a possible significant shift in the ideal launch date owing to the

introduction of constraints, and to make a preliminary estimate of the required number of additional impulses. Meanwhile, the narrow search was conducted to quantify the differences between parameters of unconstrained and constrained solutions. To address the distinct aims of the two searches, the number of optimization algorithm runs for each combination of the target asteroid, trajectory model, and constraint also differed: 150 for the broad search and 300 for the narrow search (with the exception of 1500 runs for EGA-type trajectories for Asteroid #9 owing to a very low probability of escaping local minima). Finally, 3DSMLL searches were ignored in the narrow search as the broad search results revealed that the difference between optimal 2DSMLL solutions and 3DMSLL solutions could be very small, as shall be discussed in the following subsection.

The best solution for each combination was selected as the solution with the minimum cost function value, as defined in Equations (12) or (15). In the following analyses, unless otherwise specified, a solution always refers to the best solution. Note that the maximum penalty value (defined only for constrained solutions, as the difference between the cost output and the total Δv) across all best solutions was 0.05478 km/s (corresponding to less than a constraint error of 0.234%) for the broad search and 0.00032 km/s (corresponding to less than a constraint error of 0.018%) for the narrow search.

5.2. Analysis of Broad Search Results

Using the broad search results, we first studied the number of additional impulsive maneuvers required when the approaching phase constraints were in effect. As briefly stated in Section 2.5, when seeking unconstrained fuel-optimal solutions, the addition of a new DSM to 1DSMLL-type trajectories does not generally lead to a significant improvement. However, when the constraints are reflected, the number of required maneuvers may change.

Figure 5 shows the total amount of Δv required for both unconstrained and constrained solutions. In all three panels, Δvs for the unconstrained reference (i.e., 1DSMLL-type) solutions are included for comparison with the constrained solutions. Figure 5a demonstrates that constrained solutions designed with the 1DSMLL models show a marked increase in Δv compared to the corresponding unconstrained reference solutions, indicating that these reference models are inadequate for designing constrained trajectories. However, Figure 5b,c shows that the constrained solutions reached with the 2DSMLL and 3DSMLL models can effectively limit the required magnitude of Δv to a level similar to that of the corresponding unconstrained reference solutions. It was more difficult to identify a meaningful difference between the 2DSMLL-type solutions and 3DSMLL-type solutions; the average Δv ratio of constrained 3DSMLL solutions to reference solutions was 100.90%, whilst it was 100.70% for 3DSMLL solutions (for comparison, it was 112.00% for constrained 1DSMLL solutions). Because there was only a statistically insignificant improvement that could be attained by using 2DSMLL to 3DSMLL under the current constraint setting, we decided to focus more on 2DSMLL models for the narrow search, while subsequently discussing situations that could benefit from an additional maneuver.

With respect to the shift in the optimal initial time, t_0, most constrained solutions showed only a small shift of 4.1 days (absolute values averaged without outliers), while there were 13% of the outliers with more than 100 days of shift. Upon inspection, many of these outliers appeared to have originated from the non-optimality of solutions and the multimodality of the search space (i.e., solutions with significantly different t_0 values showing a similar level of Δv) rather than a meaningful shift in the ideal launch window caused by the introduction of the constraints.

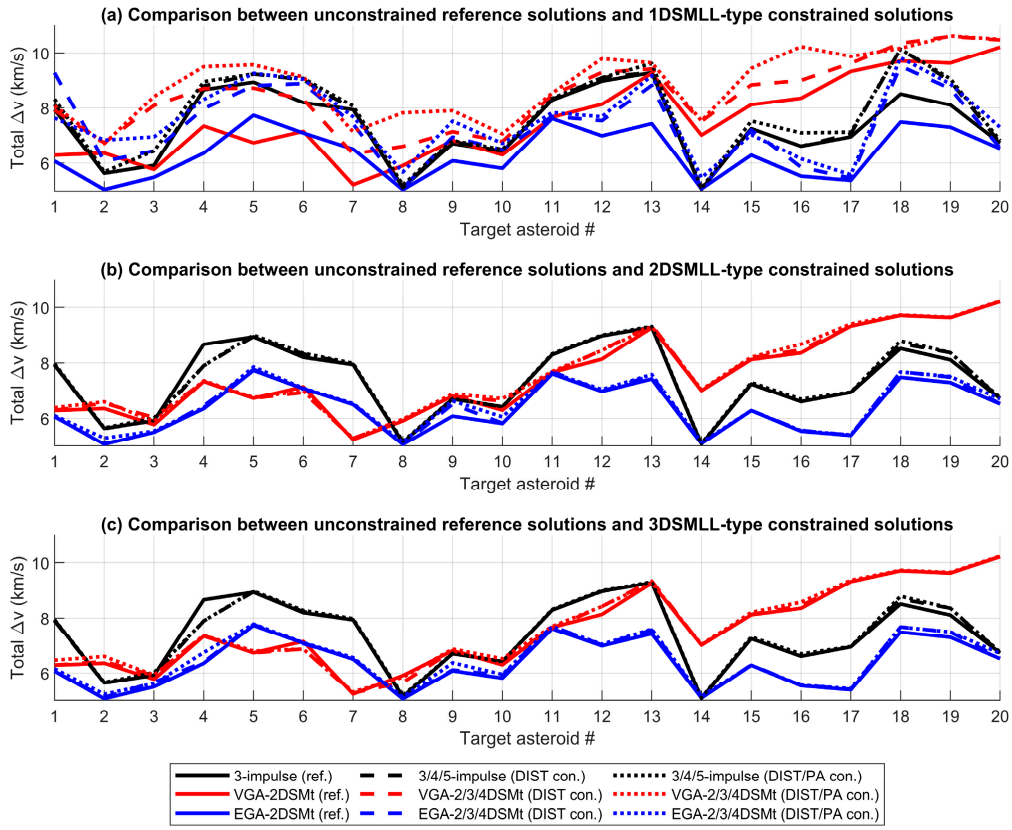

Figure 5. Comparison of total Δv value for unconstrained reference solutions and constrained solutions obtained from broad search; (**a**) 1DSMLL models, (**b**) 2DSMLL models, and (**c**) 3DSMLL models.

5.3. Analysis of Narrow Search Results

The narrow search should enable a more formal and fair comparison between unconstrained 1DSMLL solutions (i.e., reference solutions) and constrained 2DSMLL solutions, as the t_0 outliers are removed and the probability of finding suboptimal solutions is lower. A comparison of the total Δv between reference and constrained solutions is shown in Figure 6, where both the absolute difference and relative ratio of change are shown in each panel. Although the additional Δv may reach up to a few hundred meters per second in a few cases, we advise referring to Section 6 for a more thorough analysis of the increase in Δv; the narrow search results presented here have a limitation in that both the reference and constrained solutions are obtained within the fixed search space of Table 3.

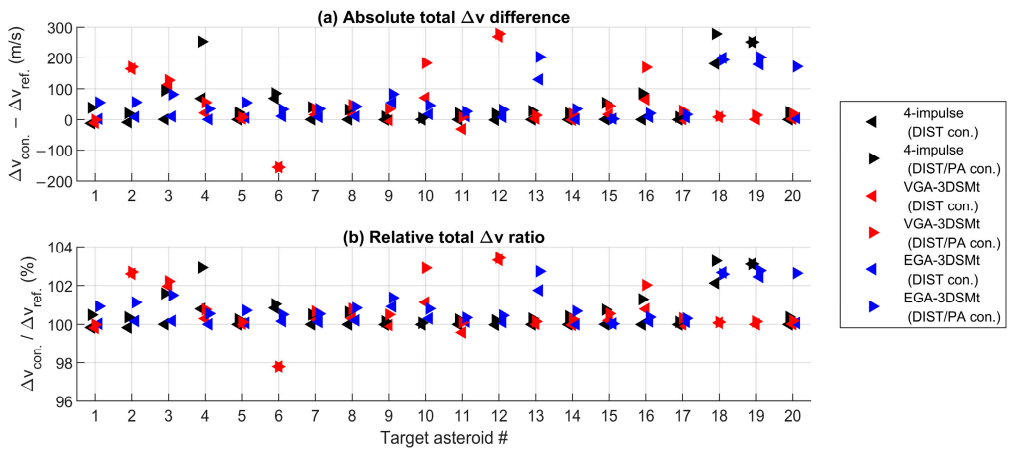

Figure 6. Comparison of total Δv value for unconstrained reference solutions and constrained solutions obtained from narrow search; (**a**) absolute change and (**b**) relative ratio of change.

Figure 7 shows the shifts in the five important trajectory parameters ($t_0, T_1, T_f,\ R_1$, and $v_{\infty,0}$), compared between reference solutions and constrained solutions. It should be noted that for the no-GA-type solutions, the TOF of the only leg is classified as T_f instead of T_1. The TOF of the last leg, denoted as T_f, was the only factor that underwent a significant shift, whereas the other four variables mostly remained close to those of the corresponding reference solution. The results confirm that when updating a reference fuel-optimal unconstrained trajectory, the bounds for the four nearly constant decision variables can be shortened to achieve a computationally efficient design; however, it may be necessary to explore a wide range of T_f values to obtain a desirable fuel-efficient constrained solution that satisfies the mission requirements.

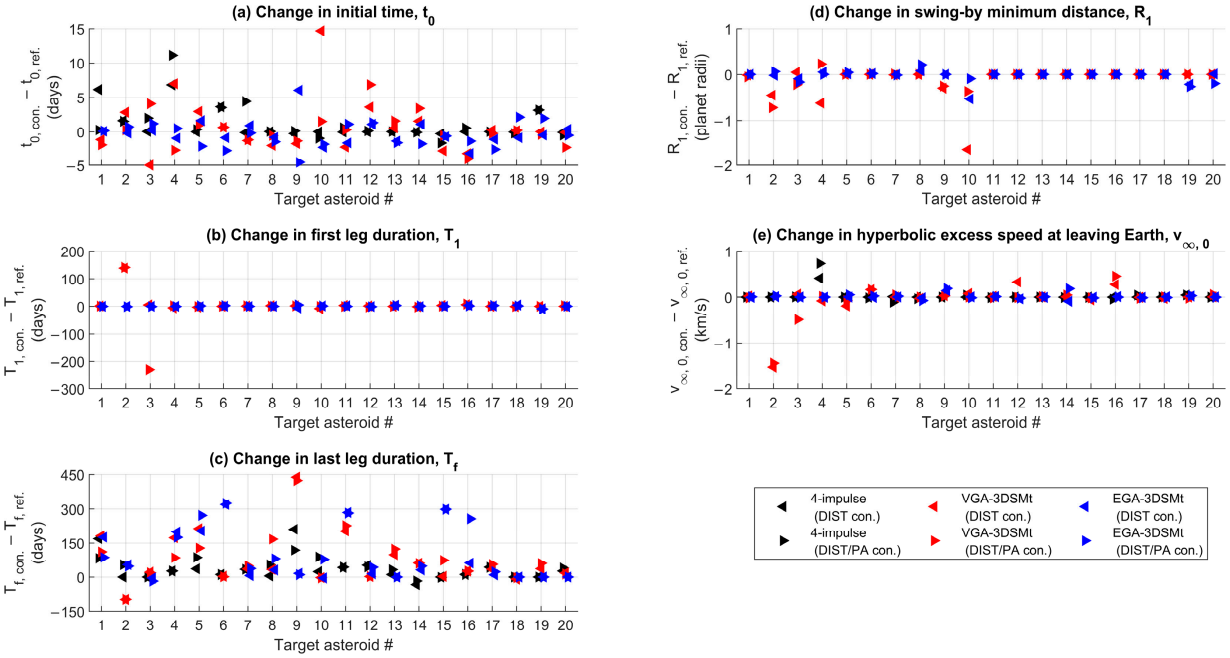

Figure 7. Changes in trajectory parameters between unconstrained reference solutions and constrained solutions obtained from narrow search: (**a**) initial time, (**b**) first leg duration, (**c**) last leg duration, (**d**) swing-by minimum distance, and (**e**) hyperbolic excess speed when leaving Earth.

The location and magnitude of the DSMs, particularly those of the last leg, are other important trajectory parameters. However, it is more difficult to quantify or visualize their changes because the related parameters are defined differently between the reference 1DSMLL models and 2DSMLL models. Furthermore, even if it is possible to quantify the trend of shifts for some DSM-related parameters, it is often difficult to control these parameters directly because of the indirect and implicit manner in which they are encoded in the design variables. However, because understanding these changes can help us better understand the general characteristics of constrained trajectories, we qualitatively analyzed the role of the additional DSM. In many cases, the added DSMs are exerted on the spacecraft near the time of the rendezvous impulse of the reference solution, and their magnitudes are slightly smaller than those of the corresponding original rendezvous impulses. These cases correspond to a situation in which the spacecraft approaches the asteroid in a trajectory similar to the reference trajectory until it applies a large braking maneuver near the asteroid before the constraints are in effect, and then slowly approaches the target asteroid. However, in other cases, it was difficult to pinpoint the newly added DSM because the maneuver timings and magnitudes were entirely redistributed within the last leg. For this reason, it is recommended that the bounds for the decision variables related to DSM timings and magnitudes are set free for constrained trajectory design.

5.4. Activation of Constraints in Constrained Trajectories

Another topic of interest is the manner in which constraints are activated in the constrained solutions. Before discussing further, in Figure 8, we present two examples (EGA-type trajectories to Asteroids #1 and #9) that show variations in the trajectories of approach for constrained and unconstrained solutions in the asteroid-centered rotating frame, where the Sun is always located on the X-axis. The activation of the distance constraint can vary depending on the unconstrained reference solution. In Figure 8a, the constrained solutions prefer to remain within a very small constraint cone during the last 45 days of the transfer, whereas a larger constraint cone is preferred in Figure 8b.

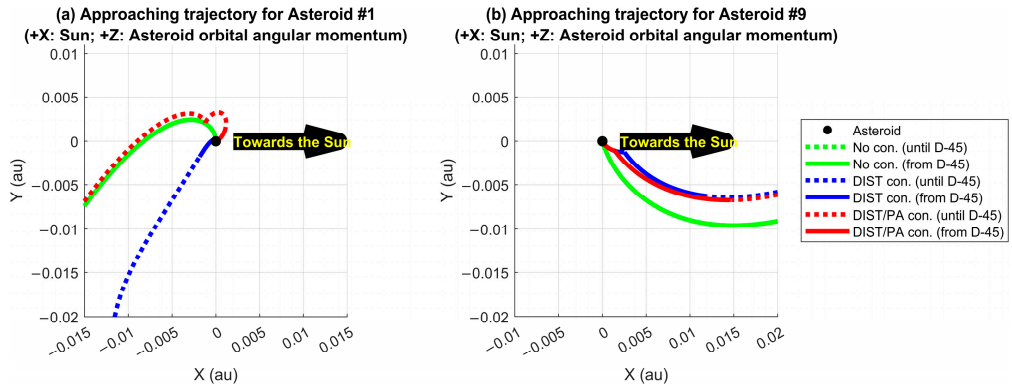

Figure 8. Comparison of the asteroid-approaching trajectories for EGA-type solutions to (**a**) Asteroid #1 and (**b**) Asteroid #9, represented in the asteroid-centered rotating frame.

With respect to the phase angle constraints, 73.3% of the phase-angle-constrained solutions neared the phase angle constraint ($\phi \geq 57°$) at least once among the three constraints checks during their final 45 days of transfer. The exact time at which the constraints were activated differed significantly depending on the approaching trajectory of the spacecraft.

To analyze the activation of the asteroid–spacecraft distance constraints, the distance at 45 days before the rendezvous was computed for all constrained solutions, and is presented in Figure 9. It is apparent from Figure 9b that when both types of constraints are applied, Δv-optimal solutions tend to minimize the distance between the asteroid and spacecraft. In other words, it is generally Δv-optimal to let the spacecraft to remain inside the smallest constraint cone possible. The exceptions to this general trend are cases where the unconstrained reference trajectories already approach the asteroid from the Sun's direction, as shown in Figure 8b. In practical applications, the maximum distance constraints can be relatively more easily defined as the maximum distance at which optical camera use can be initiated, based on camera performance and the crude estimation of the asteroid size. However, it would be more arbitrary to define the less intuitive minimum distance constraint. Nevertheless, the results presented indicate that the minimum distance constraint (or similar constraints) should be carefully selected. We further examine the influence of the constraints on the total Δv in Section 7.

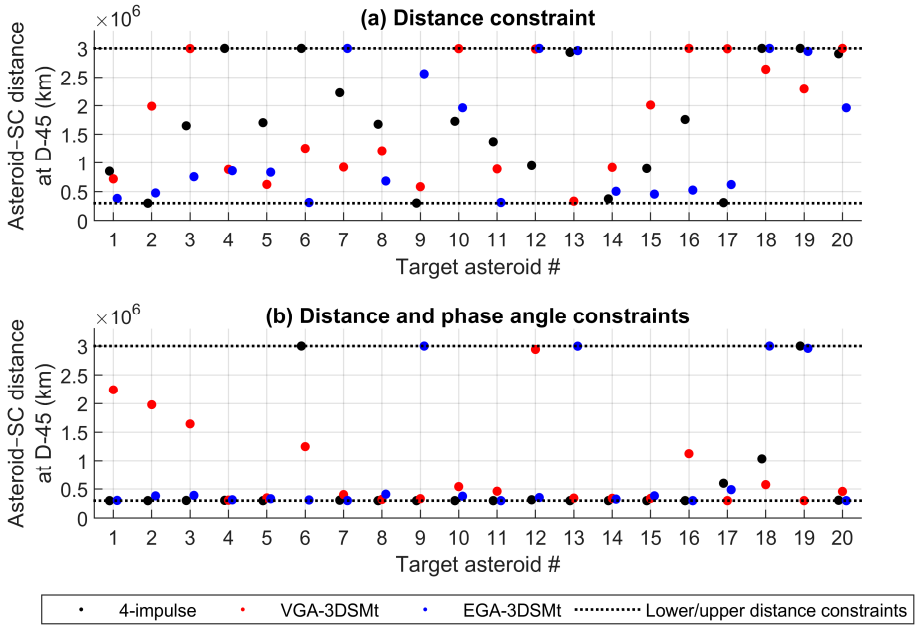

Figure 9. Asteroid–spacecraft distance at D-45 to rendezvous (**a**) when only distance constraints are applied, and (**b**) when both distance and phase angle constraints are applied.

6. Detailed Analysis on Effect of Last Leg Duration

As discussed in Section 5.3, the careful selection of the last leg duration, T_f, and maneuver-related parameters may be required to update an unconstrained reference solution to a constrained one, whereas some other major parameters (T_1, T_f, R_1, and $v_{\infty,0}$) require a lower level of discretion as their optimal values generally do not shift by a significant amount. The analysis presented in Section 5.3 demonstrated that an increase in T_f of a few hundred days is required to achieve *global* fuel optimality in some cases, which may be considered too long in terms of practicality. In fact, it is preferable to view this problem as a two-objective optimization problem in which we want to optimize both T_f and Δv in a balanced manner. Therefore, this section analyzes in more detail the effect of T_f on the total Δv.

6.1. Simulation Settings

The fuel-optimal constrained trajectories of the 2DSMLL-type were explored inside the search space neighboring the reference solutions obtained in the narrow search described in Section 5. For this analysis, we considered both distance and phase angle constraints. To effectively observe the influence of T_f, this variable was fixed at 31 different values: from −70 days to +140 days at intervals of 7 days, relative to that of the reference solution. Two other important time-related variables, namely t_0 and T_1, were fixed to those of the corresponding reference solution so that the shift in T_f became the main factor of the temporal changes. Meanwhile, bounds for $v_{\infty,0}$ and R_1 were severely limited to [90%, 110%] of the reference solution values, where the original bounds given in Table 3 take precedence when the updated bounds span beyond the original bounds. The bounds for the other variables remained unchanged from Table 3. The number of optimization runs was set differently according to the ease with which they could be solved, to five for the four-impulse model and 20 for VGA-3DSMt and EGA-3DSMt models.

6.2. Effect of Last Leg Duration on Δv

Figures 10 and 11 illustrate the relative ratio and absolute difference of the total Δv values between reference solutions to constrained solutions as a function of the amount of T_f extension. Figure 10 shows the results for Atiras and Atens, which are relatively closer to the Sun, whereas Figure 11 shows those for Apollos and Amors, which are relatively farther

from the Sun. In both figures, the vertical and horizontal black dashed lines respectively represent the last leg duration, T_f, and the total Δv of the reference solution. The most Δv-optimal solutions (among the allowed T_f values) are represented by dots with black edges. In general, a carefully chosen extension of T_f can limit the increase in the total Δv by up to 50 m/s under the current level of constraints. It should be noted that as the optimal $v_{\infty,0}$ undergoes a very minute change (Section 5.3), the additional Δv caused by introducing the approaching phase constraints is to be exerted upon mostly by the spacecraft rather than the launch system. Although this increase may be less than 1% in terms of the *total* Δv, in terms of *spacecraft* Δv it can amount to a few percent. Therefore, it is recommended that this aspect be considered during a preliminary assessment of the spacecraft mass/propellant budget.

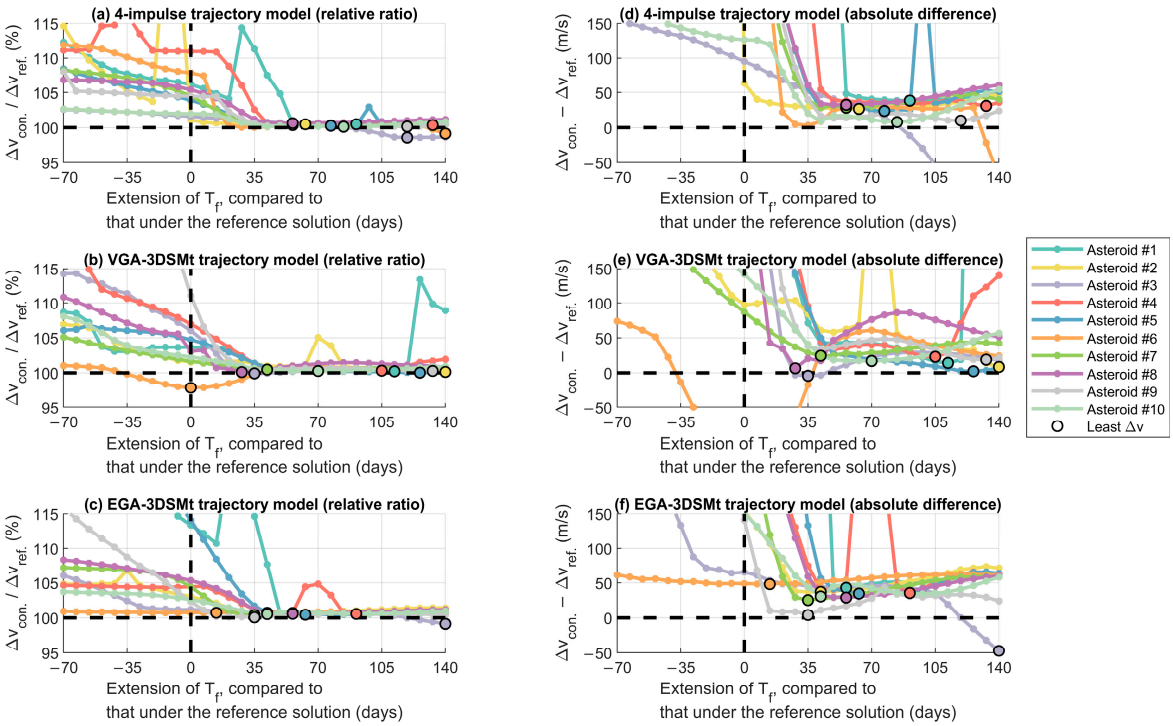

Figure 10. Relative and absolute change of total Δv as a function of last leg duration extension, compared to the unconstrained reference solution for trajectories to Asteroids #1–10 (Atiras and Atens); (**a**,**d**) no-GA-type model, (**b**,**e**) VGA-type model, and (**c**,**f**) EGA-type model.

The general trend of Δv in terms of T_f was similar in most cases; it decreased with an increasing T_f until the point at which the change became less noticeable. The relative flatness from this point on implies that solving the constrained problem directly without a reference trajectory may be an impractical choice; such a globally fuel-optimal constrained solution can sometimes require an impractically lengthy extension of the total transfer duration for a minute decrease in fuel consumption.

There are some exceptional cases that should be noted. First, as shown in Figure 10, a few solutions for Atiras-type asteroids manifested pronounced peaks that were out of the trend. This phenomenon appears to arise from the difficulty of inserting the spacecraft into the constraint cone at the right place with only a single additional maneuver. Furthermore, this phenomenon convolutes the landscape of the optimization problem, making it very difficult to acquire a truly globally optimal solution despite the smaller search space. Consequently, the solutions contained in these peaks are most likely suboptimal (i.e., not truly globally optimal within the limited search space). If the desired arrival time is near this peak, this phenomenon can be curbed by adding a new maneuver to the trajectory model, as will be shown in the next section.

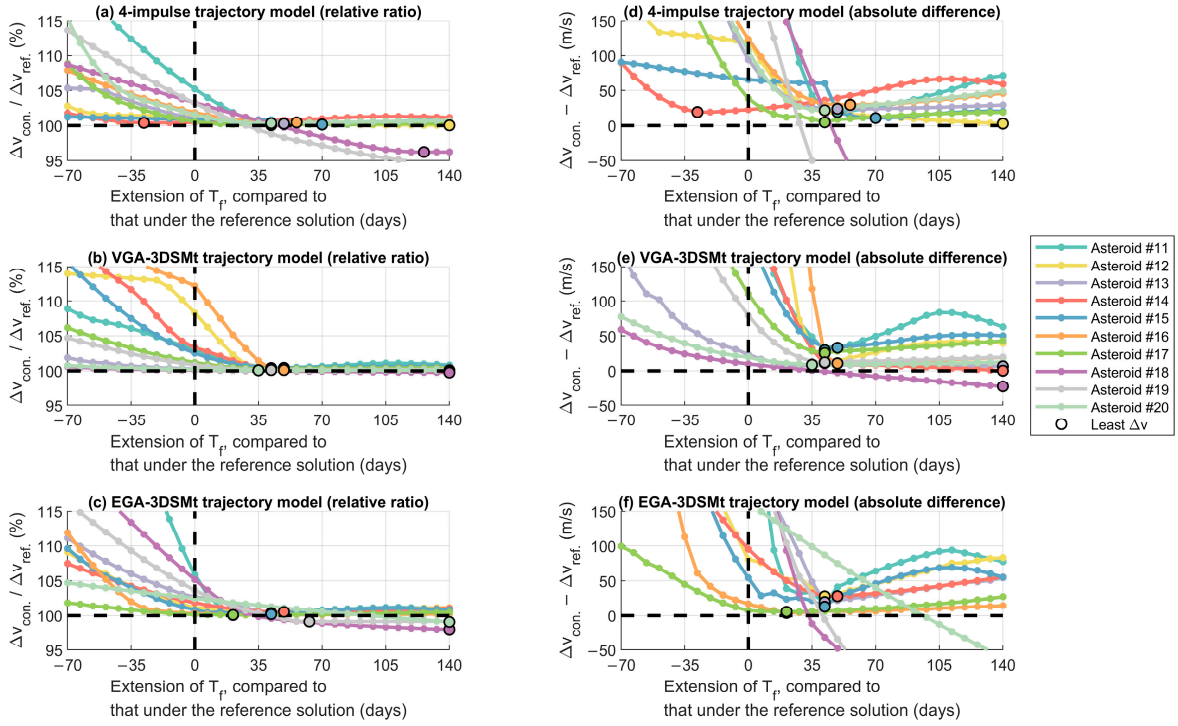

Figure 11. Relative and absolute change of total Δv as a function of last leg duration extension, compared to the unconstrained reference solution for trajectories to Asteroids #11–20 (Apollos and Amors); (**a**,**d**) no-GA-type model, (**b**,**e**) VGA-type model, and (**c**,**f**) EGA-type model.

Another interesting phenomenon is the decrease in the constrained solution's total Δv to below that of the reference solution as T_f increases, which can also be observed in Figure 6. This is believed to occur when the last leg is sufficiently long to require two major impulses for fuel optimality [28]; the reference solution itself may sometimes require two DSMs in the last leg for fuel optimality (e.g., VGA-type solution for Asteroid #6), or an increase in T_f can cause it to occur (e.g., EGA-type solution for Asteroid #3). In these trajectories, the DSM added to the last leg can simultaneously act as a maneuver for inserting the spacecraft into the constraint cone and as a maneuver that improves fuel consumption compared to the 1DSMLL-type reference solution. Therefore, if necessary, trajectory designers may attempt a few options to arrive at a new reference trajectory, such as (a) designing a reference trajectory with two DSMs in the last leg, (b) obtaining a reference trajectory with a shortened bound on T_f, or (c) acquiring a reference trajectory with a new gravity assist that splits the lengthy last leg into two legs.

7. Effect of Phase Angle and Minimum Distance Constraint

In this section, the combined effect of the maximum phase angle and minimum distance constraints is discussed. As briefly stated in Section 2.4, the minimum distance constraint was introduced because, without this limit, the Δv-optimal phase-angle-constrained solution is often reduced to a trivial solution, where the spacecraft performs a rendezvous with the asteroid using what is supposed to be the final DSM, and simply follows the asteroid thereafter until it eventually performs a virtually zero-magnitude rendezvous maneuver. This trivial solution requires basically the same Δv as the unconstrained reference solution does, but cannot be realized for actual missions because it fails to satisfy the original purpose of the gentle approach.

To evaluate the constraints' effect on the total Δv, EGA-3DSMt and EGA-4DSMt solutions for Asteroids #4 and #10 were obtained for different constraint combinations. The total Δv comparisons for trajectories to Asteroids #4 and #10 are presented in Figures 12 and 13, respectively, in the same format as in Figures 10 and 11. Examples of trajectories for different

minimum distance constraints are illustrated in Figure 14. As expected, when there is no minimum distance limit (red and yellow lines in Figures 12 and 13), the constrained solutions essentially require the same amount of fuel as the reference solution does, as long as a sufficient extension of T_f is guaranteed.

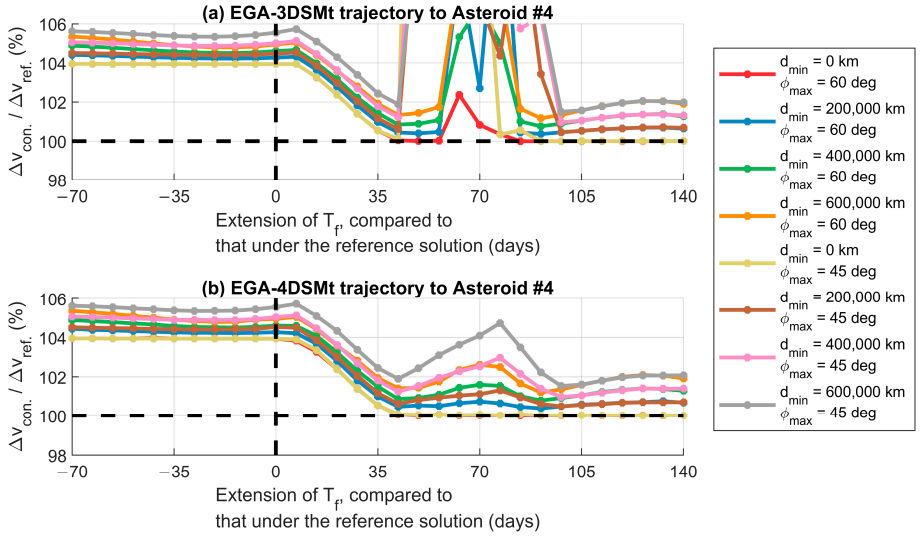

Figure 12. Change of total Δv as a function of last leg duration extension, compared to the reference solution for trajectories to Asteroid #4, for different minimum distance and maximum phase angle constraints.

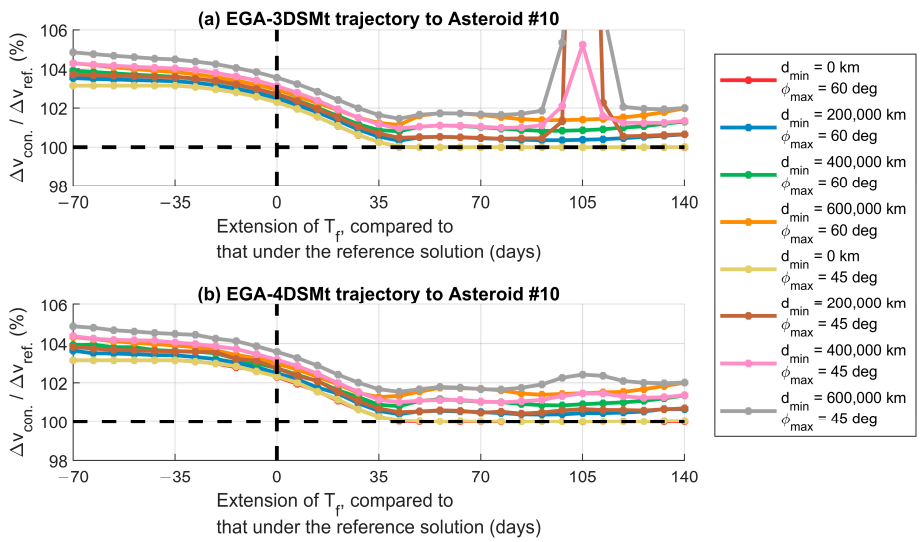

Figure 13. Change of total Δv as a function of last leg duration extension, compared to the reference solution for trajectories to Asteroid #10, for different minimum distance and maximum phase angle constraints.

Meanwhile, both a tighter minimum distance constraint (i.e., an increase in the minimum distance) and a tighter phase angle constraint (i.e., a decrease in the maximum phase angle) contribute to an increase in total Δv by requiring the trajectory to be contained inside a smaller constraint cone. These harsher constraints can also give rise to the peak phenomenon discussed in Section 6.2, as shown in Figures 12a and 13a, which can be alleviated by adding a new maneuver, as can be seen in Figures 12b and 13b. In the example trajectories shown in Figure 14b, these small additional braking maneuvers are applied inside the constraint cone, preventing the spacecraft from violating the phase angle constraint.

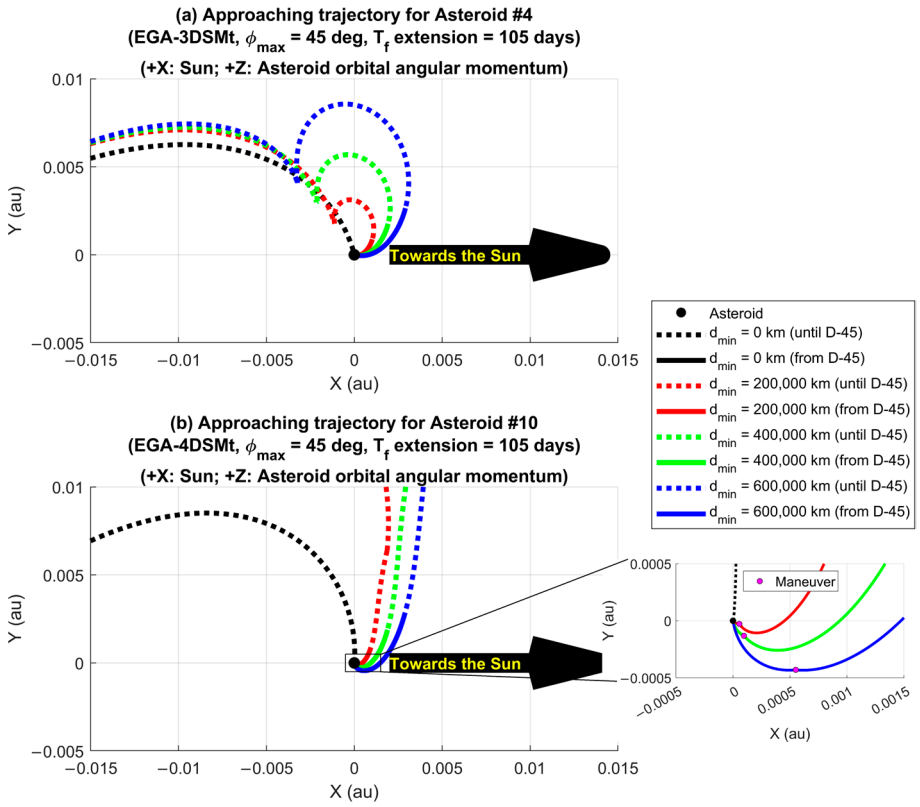

Figure 14. Comparison of approaching trajectories to (**a**) Asteroid #4 and (**b**) Asteroid #10 for different minimum distance constraints, represented in the asteroid-centered rotating frame.

Thus, these results indicate that selecting a minimum distance constraint (which, in the fuel-optimal solution, is highly likely to equal the distance at the timing of the distance constraint check) can often be important in the preliminary trajectory design phase and may need to be one of the parameters that should be considered in trade-off analysis.

8. Implications for Preliminary Trajectory Design Process for NEA Missions

Based on the analyses presented in Sections 5–7, this section discusses how they should be reflected in the preliminary trajectory design process for NEA missions. Although a fuel-optimal preliminary trajectory design under approaching phase constraints can be directly performed as single-step constrained global optimization without a reference trajectory, the increased complexity of the optimization problem and heavily perturbed problem landscape may hinder the identification of the globally optimal solution and important trajectory parameters, such as the ideal launch window. Furthermore, the analysis in Section 6.2 revealed that a globally fuel-optimal constrained solution may require an unnecessarily long mission duration to achieve a negligible improvement in fuel consumption.

Therefore, it would be ideal to view this problem as a two-objective optimization problem, where the goal is to find a mission-adequate combination of the transfer duration and total Δv (or spacecraft Δv). The two-step design approach illustrated in Figure 15 can assist in achieving a rapid constrained trajectory design and trade-off analysis. First, a fuel-optimal unconstrained solution is sought using the 1DSMLL models within a broad search space of the decision variables. Using this reference solution as a baseline to limit the search space effectively, constrained solutions are to be designed for several different values of T_f. A trade-off analysis between mission duration and Δv usage can be performed using the obtained trajectory solutions, as in Figures 10–14. In addition, this analysis can also hint at the need for an additional maneuver for reducing the constraint error or an update in the reference trajectory.

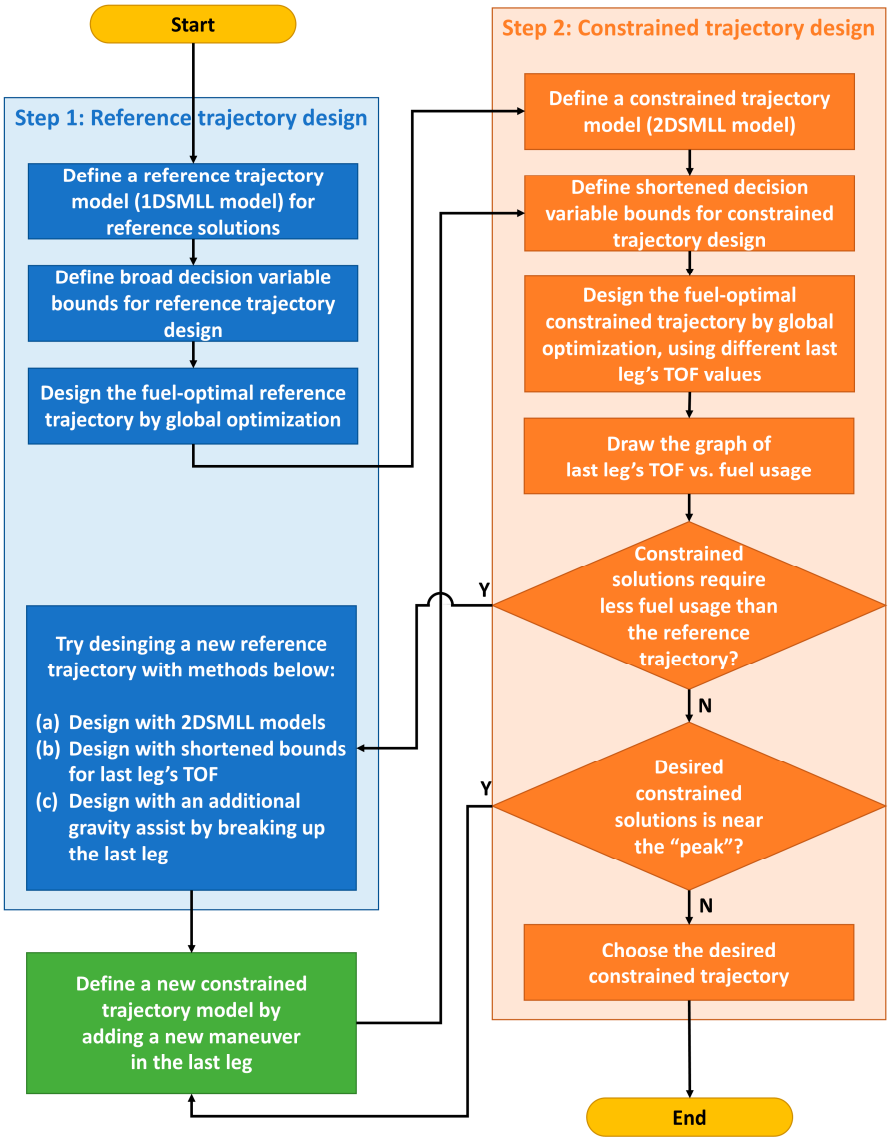

Figure 15. Proposed procedure of preliminary trajectory design for NEA missions under approaching phase constraints.

The obtained preliminary constrained solution can then be realized into a high-fidelity design or further updated by adding another few small maneuvers to fulfill other requirements. For instance, additional maneuvers inside the constraint cone can be used to improve optical navigation observability, or ensure robust arrival regardless of different launch times, as applied to the OSIRIS-REx trajectory design [17].

9. Conclusions

This paper discusses the preliminary design of interplanetary trajectories for near-Earth asteroids (NEAs), where the basic requirements for the approaching phase trajectory, namely asteroid–spacecraft distance and phase angle constraints, are reflected in the overall trajectory design process as constraints. The optimization of the overall transfer trajectory (instead of designing only the approaching trajectory as an independent problem) enables a clearer evaluation of the influence of constraints on the overall trajectory and propellant use.

To compare the characteristics of the Δv-optimal unconstrained (i.e., reference) and constrained trajectories, they were obtained using a global optimization algorithm in the same search space. Several comparisons between the solutions revealed that a fuel-optimal constrained trajectory can be efficiently obtained by adding a few deep-space

maneuvers in the last leg and increasing the time of flight of the last leg of the reference solution by an adequate amount. DSM-related parameters may also change significantly between unconstrained and constrained solutions, but their trend of change is often not straightforward; thus, it is advised that the bounds for the DSM-related decision variables be set free during the constrained trajectory design. Meanwhile, the optimal values for other important variables, such as the launch window, characteristic energy of the launch, and durations of the other legs, do not significantly differ between the unconstrained and constrained solutions, enabling trajectory designers to effectively limit their bounds during the constrained trajectory design step for time-efficient optimization.

Based on further analysis, we demonstrated the need for a trade-off analysis between transfer duration and fuel usage, as well as the constraints. As their influence can be rather subtle, such a trade-off analysis can provide better insight into constrained trajectory design than can single-step constrained trajectory optimization. Furthermore, we identified two atypical behaviors that a transfer duration vs. fuel usage trade-off graph could manifest, which may signal trajectory designers to redesign the reference trajectory or add a new braking maneuver for the constrained trajectory. Based on these findings, we present a practical two-step approach for designing approaching-phase-constrained trajectories using global optimization algorithms. The resultant preliminary constrained trajectory can then be updated into a high-fidelity trajectory or further modified by inserting additional small DSMs to improve other aspects of the mission, such as optical navigation observability.

Author Contributions: Methodology, software, and writing—original draft, P.K.; supervision, writing—review and editing, S.-Y.P. All authors have read and agreed to the published version of the manuscript.

Funding: This research was supported by the Korea Astronomy and Space Science Institute under the R&D program (Project No. 2023-1-904-00) supervised by the Ministry of Science and ICT.

Data Availability Statement: The data presented in this study are available on request from author P.K.

Conflicts of Interest: The authors declare no conflict of interest.

References

1. Conway, B.A. The problem of spacecraft trajectory optimization. In *Spacecraft Trajectory Optimization*; Conway, B.A., Ed.; Cambridge University Press: New York, NY, USA, 2010; pp. 1–15, ISBN 978-1-1076-5382-5. [CrossRef]
2. Morante, D.; Rivo, M.S.; Soler, M. A survey on low-thrust trajectory optimization approaches. *Aerospace* **2021**, *8*, 88. [CrossRef]
3. Vinkó, T.; Izzo, D. *Global Optimisation Heuristics and Test Problems for Preliminary Spacecraft Trajectory Design*; ACT-TNT-MAD-GOHTPPSTD; European Space Agency Advanced Concepts Team: Noordwijk, The Netherlands, 2008.
4. Ceriotti, M. Global Optimisation of Multiple Gravity Assist Trajectories. Ph.D. Thesis, University of Glasgow, Glasgow, UK, 2010.
5. Vasile, M.; De Pascale, P. Preliminary design of multiple gravity-assist trajectories. *J. Spacecr. Rocket.* **2006**, *43*, 794–805. [CrossRef]
6. Englander, J.A.; Conway, B.A.; Williams, T. Automated mission planning via evolutionary algorithms. *J. Guid. Control Dyn.* **2012**, *35*, 1878–1887. [CrossRef]
7. Izzo, D.; Hennes, D.; Riccardi, A. Constraint handling and multi-objective methods for the evolution of interplanetary trajectories. *J. Guid. Control Dyn.* **2015**, *38*, 792–799. [CrossRef]
8. Vasile, M.; Minisci, E.; Locatelli, M. Analysis of some global optimization algorithms for space trajectory design. *J. Spacecr. Rocket.* **2010**, *47*, 334–344. [CrossRef]
9. Vasile, M.; Minisci, E.; Locatelli, M. An inflationary differential evolution algorithm for space trajectory optimization. *IEEE Trans. Evol. Comput.* **2011**, *15*, 267–281. [CrossRef]
10. Kim, P. A Modified Basin Hopping Method for Interplanetary Trajectory Design. Master's Thesis, Yonsei University, Seoul, Republic of Korea, 2019.
11. Choi, J.H.; Lee, J.; Park, C. Deep-space trajectory optimizations using differential evolution with self-learning. *Acta Astronaut.* **2022**, *191*, 258–269. [CrossRef]
12. Gad, A.; Abdelkhalik, O. Hidden genes genetic algorithm for multi-gravity-assist trajectories optimization. *J. Spacecr. Rockets* **2011**, *48*, 629–641. [CrossRef]
13. Kawaguchi, J.; Fujiwara, A.; Uesugi, T. Hayabusa—Its technology and science accomplishment summary and Hayabusa-2. *Acta Astronaut.* **2008**, *62*, 639–647. [CrossRef]
14. Watanabe, S.; Tsuda, Y.; Yoshikawa, M.; Tanaka, S.; Saiki, T.; Nakazawa, S. Hayabusa2 mission overview. *Space Sci. Rev.* **2017**, *208*, 3–16. [CrossRef]

15. Lauretta, D.S.; Balram-Knutson, S.S.; Beshore, E.; Boynton, W.V.; Drouet d'Aubigny, C.; DellaGiustina, D.N.; Enos, H.L.; Golish, D.R.; Hergenrother, C.W.; Howell, E.S.; et al. OSIRIS-REx: Sample return from asteroid (101955) Bennu. *Space Sci. Rev.* **2017**, *212*, 925–984. [CrossRef]
16. Leonard, J.M.; Geeraert, J.L.; Page, B.R.; French, A.S.; Antreasian, P.G.; Adam, C.D.; Wibben, D.R.; Moreau, M.C.; Lauretta, D.S. OSIRIS-REx orbit determination performance during the navigation campaign. In Proceedings of the 2019 AAS/AIAA Astrodynamics and Specialist Conference, Portland, ME, USA, 11–15 August 2019.
17. Williams, B.; Antreasian, P.; Carranza, E.; Jackman, C.; Leonard, J.; Nelson, D.; Page, B.; Stanbridge, D.; Wibben, D.; Williams, K.; et al. OSIRIS-REx flight dynamics and navigation design. *Space Sci. Rev.* **2018**, *214*, 69. [CrossRef]
18. Cheng, A.F.; Rivkin, A.S.; Michel, P.; Atchison, J.; Barnouin, O.; Benner, L.; Chabot, N.L.; Ernst, C.; Fahnestock, E.G.; Kueppers, M.; et al. AIDA DART asteroid deflection test: Planetary defense and science objectives. *Planet. Space Sci.* **2018**, *157*, 104–115. [CrossRef]
19. Michel, P.; Küppers, M.; Bagatin, A.C.; Carry, B.; Charnoz, S.; de Leon, J.; Fitzsimmons, A.; Gordo, P.; Green, S.F.; Hérique, A.; et al. The ESA Hera mission: Detailed characterization of the DART impact outcome and of the binary asteroid (65803) Didymos. *Planet. Sci. J.* **2022**, *3*, 160. [CrossRef]
20. Ozaki, N.; Yamamoto, T.; Gonzalez-Franquesa, F.; Gutierrez-Ramon, R.; Pushparaj, N.; Chikazawa, T.; Dei Tos, D.A.; Çelik, O.; Marmo, N.; Kawakatsu, Y.; et al. Mission design of DESTINY+: Toward active asteroid (3200) Phaethon and multiple small bodies. *Acta Astronaut.* **2022**, *196*, 42–56. [CrossRef]
21. Kim, P.; Park, S.-Y.; Cho, S.; Jo, J.H. A preliminary impulsive trajectory design for (99942) Apophis rendezvous mission. *J. Astron. Space Sci.* **2021**, *38*, 105–117. [CrossRef]
22. Wang, J.; Li, H.; Lin, Z.; Huo, H. Time-fixed glideslope guidance for approaching the proximity of an asteroid. *Aerospace* **2021**, *8*, 137. [CrossRef]
23. Qiao, D.; Zhou, X.; Zhao, Z.; Qin, T. Asteroid approaching orbit optimization considering optical navigation observability. *IEEE Trans. Aerosp. Electron. Syst.* **2022**, *58*, 5165–5179. [CrossRef]
24. Yuan, H.; Li, D.; Wang, J. Hybrid guidance optimization for multipulse glideslope approach with bearing-only navigation. *Aerospace* **2022**, *9*, 242. [CrossRef]
25. Luo, Y.-Z.; Lei, Y.-J.; Tang, G.-J. Optimal multi-objective nonlinear impulsive rendezvous. *J. Guid. Control Dyn.* **2007**, *30*, 994–1002. [CrossRef]
26. Kawakatsu, Y. V∞ direction diagram and its application to swingby design. In Proceedings of the 21st International Symposium on Space Flight Dynamics, Toulouse, France, 28 September–2 October 2009.
27. Vavrina, M.A.; Englander, J.A.; Ellison, D.H. Global optimization of n-maneuver, high-thrust trajectories using direct multiple shooting. In Proceedings of the 26th AAS/AIAA Space Flight Mechanics Meeting, Napa, CA, USA, 14–18 February 2016.
28. Taheri, E.; Junkins, J.L. How many impulses redux. *J. Astronaut. Sci.* **2020**, *67*, 257–334. [CrossRef]
29. Wales, D.J.; Doye, J.P.K. Global optimization by basin-hopping and the lowest energy structures of Lennard-Jones clusters containing up to 110 atoms. *J. Phys. Chem. A* **1997**, *101*, 5111–5116. [CrossRef]
30. Addis, B.; Cassioli, A.; Locatelli, M.; Schoen, F. A global optimization method for the design of space trajectories. *Comput. Optim. Appl.* **2011**, *48*, 635–652. [CrossRef]
31. Martí, R.; Lozano, J.A.; Mendiburu, A.; Hernando, L. Multi-start methods. In *Handbook of Heuristics*; Martí, R., Pardalos, P.M., Resende, M.G.C., Eds.; Springer: Cham, Germany, 2018; pp. 155–175, ISSN 978-3-3190-7123-7. [CrossRef]
32. McCarthy, S.L.; McGuire, M.L. Parallel monotonic basin hopping for low thrust trajectory optimization. In Proceedings of the 28th AAS/AIAA Space Flight Mechanics Meeting, Kissimmee, FL, USA, 8–12 January 2018.
33. Small-Body Orbits & Ephemerides. Available online: https://ssd.jpl.nasa.gov/sb/orbits.html (accessed on 15 August 2022).
34. Horizons System. Available online: https://ssd.jpl.nasa.gov/horizons/app.html (accessed on 15 August 2022).
35. Meeus, J. *Astronomical Algorithms*, 1st ed.; Willmann-Bell: Richmond, VA, USA, 1991; p. 315, ISBN 978-0-9433-9635-4.